Vol 460|23 July 2009|doi:10.1038/nature08173

LETTERS

Near-field focusing and magnification through self-assembled nanoscale spherical lenses

Ju Young Lee[1]*, Byung Hee Hong[1,2]*, Woo Youn Kim[1], Seung Kyu Min[1], Yukyung Kim[1], Mikhail V. Jouravlev[1], Ranojoy Bose[3], Keun Soo Kim[2], In-Chul Hwang[1], Laura J. Kaufman[4], Chee Wei Wong[3], Philip Kim[5] & Kwang S. Kim[1]

It is well known that a lens-based far-field optical microscope cannot resolve two objects beyond Abbe's diffraction limit. Recently, it has been demonstrated that this limit can be overcome by lensing effects driven by surface-plasmon excitation[1–3], and by fluorescence microscopy driven by molecular excitation[4]. However, the resolution obtained using geometrical lens-based optics without such excitation schemes remains limited by Abbe's law even when using the immersion technique[5], which enhances the resolution by increasing the refractive indices of immersion liquids. As for submicrometre-scale or nanoscale objects, standard geometrical optics fails for visible light because the interactions of such objects with light waves are described inevitably by near-field optics[6]. Here we report near-field high resolution by nanoscale spherical lenses that are self-assembled by bottom-up integration[7] of organic molecules. These nanolenses, in contrast to geometrical optics lenses, exhibit curvilinear trajectories of light, resulting in remarkably short near-field focal lengths. This in turn results in near-field magnification that is able to resolve features beyond the diffraction limit. Such spherical nanolenses provide new pathways for lens-based near-field focusing and high-resolution optical imaging at very low intensities, which are useful for bio-imaging, near-field lithography, optical memory storage, light harvesting, spectral signal enhancing, and optical nano-sensing.

Miniaturized lenses are often found in biological systems[8,9], and have been widely used for optical microelectromechanical systems[10]. Despite numerous studies of miniaturized lenses[11–14], no serious studies have been undertaken of lenses for subwavelength nano-optics. To this end, we fabricate well-defined nanoscale lenses of calix[4]hydroquinone (CHQ), which is composed of four *p*-hydroquinone subunits with eight hydroxyl groups[15]. Intermolecular short hydrogen-bonding[16] and $\pi-\pi$ stacking interactions[17] are very useful forces for self-assembling supramolecular CHQ nanostructures[18]. One class of such self-assembled nanostructures is represented by sphere-derived shapes of diameter 50 nm to 3 μm, as seen in scanning electron microscopy (SEM) images (Fig. 1a–c). Dissolving the CHQ monomers in 1:1 water–acetone solution leads to the formation of needle-like CHQ nanotube crystals with infinitely long hydrogen-bonded arrays. As the crystals grown at –14 °C are heated at 40 °C in aqueous environments for a day, CHQ molecules released from the crystals re-assemble into nanospheres.

At the beginning of this process, film-like structures of CHQ cover the surface of the crystals. CHQ molecules released from the surface accumulate in a small volume under the film, leading to the nucleation and growth of two-dimensional disk-shaped structures. Spherical curvatures are then gradually formed, as more of the released CHQ molecules re-assemble in three dimensions. These are intermediate structures of anisotropically growing spheres (see Supplementary Information A for the mechanism). These 'plano-spherical convex' (PSC) structures—with a spherical face on one side and a flat face on the other side—can be isolated, and these CHQ lenses are stable in air. The negative electron beam resist properties of calixarene-based structures[19] are used for fabrication and positioning of optical devices using these CHQ lenses (Supplementary Information D). Although these experiments are technically sophisticated, the intricately self-assembled nanolenses enable us to study the physics of nanolens optics.

The size distribution of CHQ lenses can be controlled by the time and temperature of the self-assembly process. Typically, PSC lenses

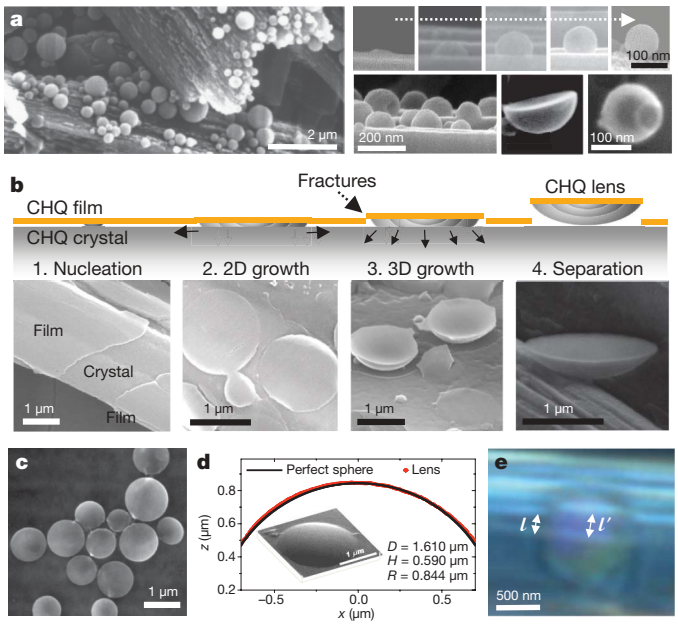

Figure 1 | CHQ plano-spherical convex lenses. a, SEM images of growing CHQ nanospheres and their intermediate structures. **b**, Schematic diagrams and SEM images showing the self-assembly of CHQ lenses (see text for details). **c**, SEM image showing various sizes of CHQ lenses separated as an aqueous suspension and drop-dried on a substrate. **d**, AFM profile showing the near perfect spherical face of the lens. Inset, corresponding SEM image. **e**, Optical microscope image of CHQ lenses on a CHQ nanotube crystal, showing the magnification by the lens. The line spacing (*l*) behind the lens is considerably increased (*l*′).

[1]Center for Superfunctional Materials, Department of Chemistry, Pohang University of Science and Technology, Hyojadong, Namgu, Pohang 790-784, Korea. [2]Department of Chemistry and SKKU Advanced Institute of Nanotechnology, Sungkyunkwan University, Suwon 440-746, Korea. [3]Department of Mechanical Engineering, [4]Department of Chemistry, [5]Department of Physics, Columbia University, New York, New York 10027, USA.
*These authors contributed equally to this work.

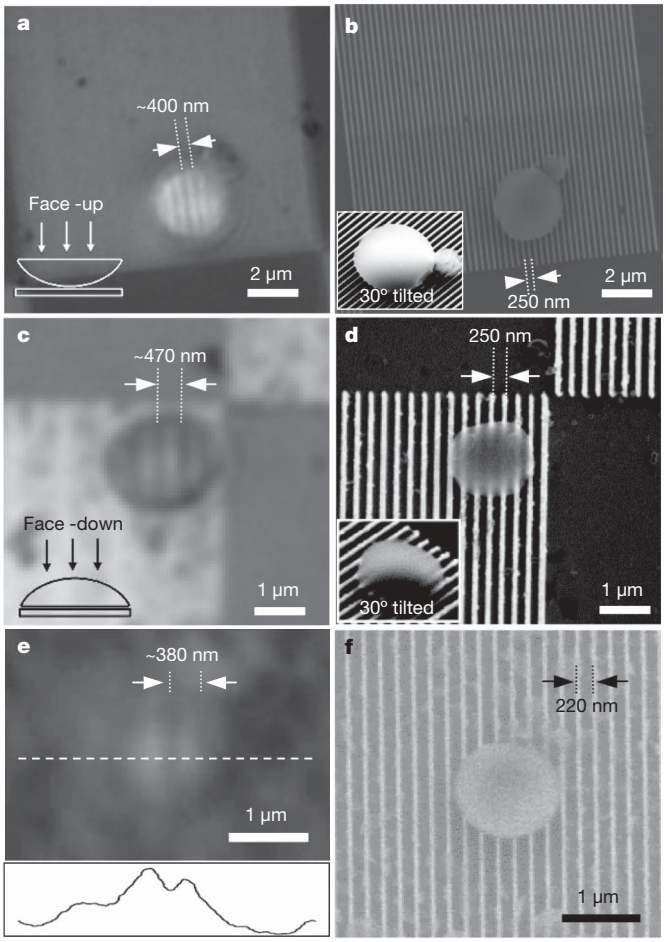

Figure 2 | Optical microscope/SEM images of CHQ lenses on patterned substrates. **a**, Optical microscope image of a face-up lens placed on a glass substrate with Pd stripe patterns (see Supplementary Information C for more images taken with different focus and magnification). **b**, SEM image corresponding to **a**. Inset, image of tilted lens. **c**, Optical microscope image of a face-down lens. **d**, SEM image corresponding to **c**. **e**, Optical microscope image of a face-up lens. Inset, light intensity profile taken from the blue dotted line. **f**, SEM image corresponding to **e**. The sub-diffraction-limit patterns cannot be resolved in conventional optical microscopy, but the magnifying effect through the lens allows the stripe patterns of 250/220 nm spacing to be resolved.

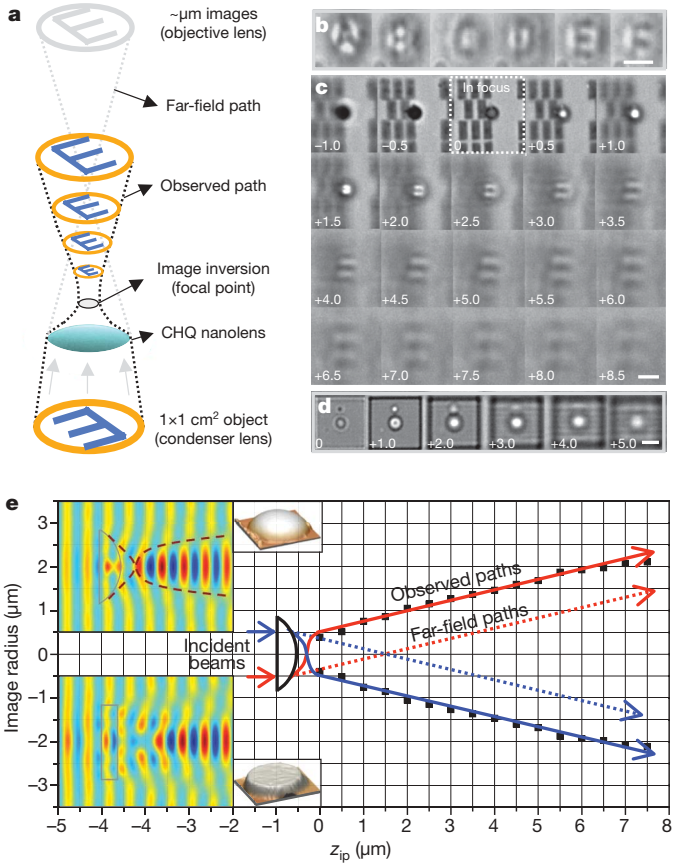

Figure 3 | Optical images and beam trajectories of alphabetical characters projected through CHQ lenses and PMMA disks. **a**, Schematic illustration of the imaging process. The light sources transmitting a patterned glass are collimated by a condenser lens. As the nanolens focuses the beam, inverted images are formed after passing through the focal point. Each slice of the images is obtained at a distance z_{ip} from the lens/disk bottom. **b**, Optical microscope images of various inverted alphabetical characters (A–F) projected through the lens. The upright non-inverted characters are imaged due to the image inversion at the image plane ~3.5 μm away from the nanolens. **c**, Optical microscope images of the alphabetical character "E" projected through a CHQ lens ($D = 1.7$ μm, $H = 480$ nm) on vertical image planes at varying distances z_{ip}. The number in each slice denotes the value of z_{ip}. 'In-focus' denotes the image focused on the plane of the Pd stripe patterns. **d**, Projected optical microscope images through a 1.7-μm-wide and 400-nm-thick PMMA disk, which shows no clear alphabetical character image formation. **e**, Beam trajectory with reduced focal length in the near-field PSC lens. Small insets on the left, AFM images of the CHQ lens (upper) and the PMMA disk (lower). Large insets on the left, FDTD simulation results of the radial component of the electric field (E_x) of the PSC lens (upper) and the PMMA disk (lower) ($\lambda = 472$nm). All scale bars, 2 μm.

with nanoscale thickness $H < 800$ nm and diameter $D = 0.05$–3 μm can be synthesized and separated from the aqueous suspension for further experiments. Surface roughness of the lenses deposited on a SiO/Si substrate is determined by an atomic force microscope (AFM). The round surface exhibits a typical deviation from a spherical surface of less than 3% with a surface roughness of <1 nm (Fig. 1d). The nearly perfect PSC structure demonstrates that self-assembled CHQ lenses are high-quality optical elements.

Figure 1e shows an optical microscope image of a CHQ lens ($D = 970$ nm, $H = 220$ nm) on top of CHQ tubule bundles under filtered light ($\lambda_{max} = 472$ nm) from a halogen lamp. The image indicates that the lens magnifies the underlying object with a magnification factor M ($= l'/l = \sim 1.6$). The paraxial focal length estimated from the observed magnification is $F = HM/(M-1) = 590$ nm, much shorter than that expected from geometric optics, $F_{geo} = R/(n-1) = 1.3$ μm (R, lens radius; $n = 1.5$, refractive index). The deviations from geometrical optics for the subwavelength-size CHQ lenses are the key signature of near-field focusing. The reduction of the focal length in the CHQ nanolens implies enhanced magnifying effects through the nanolens.

To demonstrate enhanced spatial resolution, we further investigate the optical properties of CHQ lenses on pre-fabricated subwavelength objects as follows (Fig. 2). First, 250- and 220-nm pitch metallic (Pd/Cr, 120/3 nm thick) stripe arrays are fabricated by electron beam lithography on glass substrates. The CHQ lenses isolated in aqueous suspensions (Fig. 1c) are randomly placed on the patterned substrate by spinning (Fig. 2b, d, f). We use a high resolution optical microscope to take reflection mode images of the same part of the sample (Fig. 2a, c, e). The optical images were obtained through a 100× objective lens with a numerical aperture (NA) of 0.9. The Rayleigh resolution limit for point objects ($r = 0.61\lambda$/NA) is 320 nm, while that for line objects ($r = 0.5\lambda$/NA) is 262 nm. A more stringent Sparrow resolution limit ($r = 0.475\lambda$/NA)[20] is 249 nm. Indeed, the optical images outside the CHQ lenses do not resolve the underlying metallic stripes, as the stripe spacings of $d = 220$ and 250 nm are narrower than, or very similar to, the stringent resolution limit. On the other hand, resolved individual metallic stripes are clearly imaged through the CHQ lens (Fig. 2a, c for 250 nm and Fig. 2e for 220 nm). The image magnification increases as the distance

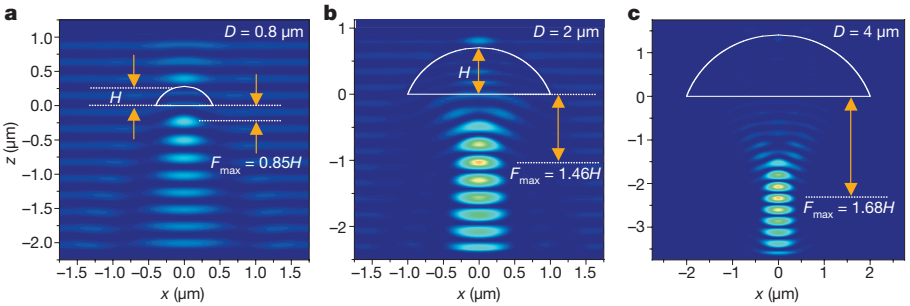

Figure 4 | Focal length changes for various sizes of CHQ lenses (fixed $H/D = 0.35$). **a**, $D = 0.8$ μm; **b**, $D = 2$ μm; **c**, $D = 4$ μm. Data were obtained from FDTD simulation results of $|E_x|^2$ ($\lambda = 472$ nm).

between nanolens and image is increased with micromanipulators and piezo-controlled nano-positioning stages. The magnifying effect enhances the resolution substantially (by as much as 2.5 times). The magnified images of the face-up lenses show pin-cushion distortion (Supplementary Information C), whereas no notable distortion appears for the face-down lens. This difference arises because the near-field image of the face-up lens is formed by the interference of the secondary Fresnel's waves on the flat and convex surfaces of the lens, while the near-field image of the face-down lens is formed by the secondary surface waves due to the convex surface.

To analyse the imaging and focusing behaviours through the CHQ lenses, we projected a series of alphabetical character images into a CHQ lens ($D = 1.7$ μm, $H = 0.48$ μm) via a condenser lens (NA = 0.8) in the far field (Fig. 3a–c). The images of "E" formed by the PSC lens (Fig. 3c) are compared with those formed by a flat disk (Fig. 3d). The transmitted images through the PSC lens or flat disk were recorded by an optical microscope with a CCD camera focused on different image planes at a distance z_{ip} from the lens/disk bottom (Supplementary Information F). In Fig. 3e, the solid lines are guides to the eye, following the square dots (which are the measured optical beam trajectories of the top and bottom edges of the "E" image along z_{ip}). The far-field optical paths calculated from geometrical ray optics (dotted lines) are also presented for comparison. As the image plane moves away from the CHQ lens, the images are inverted and magnified. In Fig. 3c, we observe clear magnified and inverted images of "E" along the axial positions for $z_{ip} \geq 1.5$–2.0 μm, and the letter shape is still seen at $z_{ip} = 1.0$ μm. At $z_{ip} < 0.5$ μm, we observe that the bright spot with a dark annular ring at $z_{ip} = 0.5$ μm changes to the grey/dark spot with a bright annular ring surrounding the dark spot. We did not observe the direct non-inverted image for $z_{ip} < 0.5$ μm. However, since the "E" image is clearly inverted for $z_{ip} \geq 1.5$ μm, we deduce that the image inversion should occur at the focal point between the two adjacent points at $z_{ip} = 0.5$ μm (lens top) and $z_{ip} = 1.0$ μm, which have the first and second smallest bright spot radii (0.38 and 0.42 μm, respectively) among many images taken at every 0.5-μm step.

As the lens height is 0.48 μm and the bright spot size at $z_{ip} = 0.5$ μm is slightly smaller than that at $z_{ip} = 1.0$ μm, the focal point is expected to be located at 0.48 μm $< z_{ip} <$ 0.75 μm (then the focal length is not more than 0.27 μm). Thus, this focal length is in agreement with the theoretically estimated focal length (0.3 μm, or $z_{ip} = \sim 0.8$ μm) assumed as the first Fresnel zone focal length ($F = 4\lambda/(\pi \mathrm{NA})^2$). Given the axial resolution limit (Rayleigh range $z_R = (4/\pi)\lambda/\mathrm{NA}^2$) of 0.9 μm according to Gaussian beam optics, the measured focal point is at $z_{ip} = \sim 0.7 \pm 0.9$ μm, or $F = \sim 0.2 \pm 0.9$ μm, much smaller than the geometrical focal length F_{geo} (2.0 μm; $z_{ip} = \sim 2.5$ μm). This drastically shortened focal length ($F \ll F_{geo}$), which should yield the curvilinear trajectories for $z_{ip} < 1.0$ μm, is supported in Fig. 3e by tracing the image size of the "E" in Fig. 3c down to $z_{ip} = 1.0$ μm. It is further clearly seen in accurate finite-difference time domain (FDTD) simulations that the inversion occurs at $z_{ip} = 0.8$ μm (Fig. 3e top left inset). Here, the images between $z_{ip} = 0.0$ μm and the focal point are in the Fresnel diffraction region, appearing as the Fourier transformed image. In this region, the asymptotic beam path is curvilinear so that the image can be inverted at the short focal point. This result explains the experiment showing the inverted image of "E" consistently obtained for $z_{ip} \geq 1.0$ μm in Fig. 3c.

Shape-dependent focusing and imaging was studied by performing a similar experiment through a patterned poly(methylmethacrylate) (PMMA) disk formed by electron beam lithography. The disk has flat surfaces on both sides, but its thickness and size are similar to those of the CHQ lens. In contrast to the clear images created through the PSC lens, the light propagating through the disk shows no clear images (Fig. 3d). These experimental images are consistent with the electromagnetic simulation (Fig. 3e bottom left inset); at $z_{ip} = \sim 0$ μm along the axis, the image has a small bright spot; at $z_{ip} = \sim 1$ μm, the image has a small dark spot at the centre and an annular bright spot; and the images for $z_{ip} \geq \sim 2$ μm again have bright spots at the centre. The difference between the images created through the PSC lens and the flat disk is thus clearly confirmed by electromagnetic simulations, and the image formation depends on the shape (surface curvature) of the optical elements. We note that the focal point of a nanolens originates mainly from surface waves at the spherical interface of the PSC lens, and the near-field focal length is drastically shortened by the interference of the propagating waves from the lens edges because the nanolens length-scale is comparable to the wavelength (Supplementary Information B). The resulting curvilinear ray path with a wave propagation to match the amplitude and phase inside and outside the lens forms a small focused spot at a very short near-field focal distance (solid lines in Fig. 3e).

To investigate the size-dependent diffraction/refraction phenomena in the near-field regime, we performed FDTD simulations[21] for sub-wavelength-size lenses of different diameters ($D = 0.8$–4 μm) with fixed ratio of $H/D = 0.35$ (Fig. 4). The incident plane waves are polarized along the x-direction, and Fig. 4 shows the spatial distribution of $|E_x|^2$ where E_x is the x-component of the electric field. As the lens size approaches the wavelength, the near-field focal length (F_{max}) showing the maximum light intensity decreases remarkably towards the first Fresnel zone. This near-field focusing is due to superposition of the diffraction on the flat aperture and the interference of secondary Fresnel waves on the spherical surface of the PSC lens, whose diameter is comparable to the wavelength of light.

Given that high resolution imaging beyond or near the diffraction limit has been achieved by relying on a stimulated-emission-depletion method, a lens-less near-field optical method, and novel materials approaches[22–26], the near-field focusing and magnification discussed here represent a complementary approach to obtaining lens-based high resolution beyond the diffraction limit at low intensities. This magnification can be further increased by using immersion lensing techniques. Such a combination would lead to hyper-refraction phenomena due to surface waves on the interfaces. Based on the merit of spherical lens-based optics, the near-field focusing and magnification phenomena in nanoscale lenses would have wide applications, including super-resolution by a nanolens array and by a nanolens on an AFM

or aperture-less near-field scanning optical microscope (ANSOM). This is possible because nanolenses at arbitrary locations can successfully be transferred to pre-determined locations by using micromanipulators with the assistance of an SEM, and fabricated in array in order to increase the area over which high spatial resolution is achieved (Supplementary Information E). In particular, the focusing and magnification effect of the nanolens would have useful applications in signal enhancements in spectroscopy—in micro-photoluminescence intensity with quantum dots for single (near-infrared) photon spectroscopy (Supplementary Information H), and in Raman intensity on substrates such as graphene[27,28] (Supplementary Information I). Application to deep ultraviolet lithography is also possible (Supplementary Information G), because regardless of the visible or ultraviolet wavelength, nanolenses can be used to obtain high resolution beyond the diffraction limit, as long as the wavelength is comparable to the lens size.

METHODS SUMMARY

CHQ nanoscale lenses are self-assembled in 1:1 acetone–water solution by evaporating the solution slowly for a few days in ambient conditions. After dissolving 10 mg CHQ monomers in 2 ml acetone solvent, 2 ml water is added. Slow evaporation of solution leads to the self-assemblies of CHQ nanostructures including CHQ lenses. Pd/Cr (120/3 nm thick, 220 and 250 nm pitch) line patterns are fabricated on a 0.13–0.16 mm thick glass substrate with e-beam lithography. After depositing chromium to a thickness of 3 nm using a thermal evaporator (BOC Auto 306, Edwards), positive electron-beam resist PMMA is spin-coated on a SiO_2 substrate at 4,000 r.p.m. The PMMA film is exposed to 30 kV electron beam and developed with MIBK:IPA = 1:3 developer for patterning. Deposition of 120 nm palladium is performed with an electron-beam evaporator (SC2000, SEMICORE), and then the patterns are accomplished through a lift-off process. We obtained the magnified image through the CHQ lens using an optical microscope equipped with micromanipulators and piezo-controlled nano-positioners (E-610, Physik Instrumente). FDTD simulations were performed using the FullWAVE 4.0 program (RSoft Design Group). In the Supplementary Information we describe relocation of CHQ lenses with a dual focused ion beam microscope (Helios Nanolab 600, FEI) and an SEM (JSM6390, Jeol). CHQ lenses are attached to the end of a tungsten tip (which is adhesive after contact with an adhesive carbon tape), and then transferred to pre-determined positions. The enhancement of Raman intensity of graphene through a CHQ lens is observed by a micro-Raman microscope (InVia Raman microscope, Renishaw; laser wavelength 633 nm, power 4 mW).

Received 30 December 2008; accepted 28 May 2009.

1. Smolyaninov, I. I., Hung, Y.-J. & Davis, C. C. Magnifying superlens in the visible frequency range. *Science* **315,** 1699–1701 (2007).
2. Liu, Z., Lee, H., Xiong, Y., Sun, C. & Zhang, X. Far-field optical hyperlens magnifying sub-diffraction-limited objects. *Science* **315,** 1686 (2007).
3. Fang, N., Lee, H., Sun, C. & Zhang, X. Sub-diffraction-limited optical imaging with a silver superlens. *Science* **308,** 534–537 (2005).
4. Hell, S. W. Far-field optical nanoscopy. *Science* **316,** 1153–1158 (2007).
5. Yano, T., Shibata, S. & Kishi, T. Fabrication of micrometer-size glass solid immersion lens. *Appl. Phys. B* **83,** 167–170 (2006).
6. Merlin, R. Radiationless electromagnetic interference: evanescent-field lenses and perfect focusing. *Science* **317,** 927–929 (2007).
7. Whitesides, G. M. & Grzybowski, B. Self-assembly at all scales. *Science* **295,** 2418–2421 (2002).
8. Aizenberg, J., Tkachenko, A., Weiner, S., Addadi, L. & Hendler, G. Calcitic microlenses as part of the photoreceptor system in brittlestars. *Nature* **412,** 819–822 (2001).
9. Lee, L. P. & Szema, R. Inspirations from biological optics for advanced photonic systems. *Science* **310,** 1148–1150 (2005).
10. Dong, L., Agarwal, A. K., Beebe, D. J. & Jiang, H. Adaptive liquid microlenses activated by stimuli-responsive hydrogels. *Nature* **442,** 551–554 (2006).
11. Yang, S. K. U., Chaitanya, T. E. L., Chen, G. & Aizenberg, J. Microlens arrays with integrated pores as a multipattern photomask. *Appl. Phys. Lett.* **86,** 201121 (2005).
12. Jeong, K.-H., Kim, J. & Lee, L. P. Biologically inspired artificial compound eyes. *Science* **312,** 557–561 (2006).
13. Fletcher, D. A., Goodson, K. E. & Kino, G. S. Focusing in microlenses close to a wavelength in diameter. *Opt. Lett.* **26,** 399–401 (2001).
14. Wu, H., Odom, T. W. & Whitesides, G. M. Connectivity of features in microlens array reduction photolithography: generation of various patterns with a single photomask. *J. Am. Chem. Soc.* **124,** 7288–7289 (2002).
15. Hong, B. H. *et al.* Self-assembled arrays of organic nanotubes with infinitely long one-dimensional H-bond chains. *J. Am. Chem. Soc.* **123,** 10748–10749 (2001).
16. Kim, K. S. *et al.* Assembling phenomena of calix[4]hydroquinone nanotube bundles by one-dimensional short hydrogen bonding and displaced π-π stacking. *J. Am. Chem. Soc.* **124,** 14268–14279 (2002).
17. Kim, K. S., Tarakeshwar, P. & Lee, J. Y. Molecular clusters of π-systems: theoretical studies of structures, spectra and origin of interaction energies. *Chem. Rev.* **100,** 4145–4186 (2000).
18. Hong, B. H., Bae, S. C., Lee, C.-W., Jeong, S. & Kim, K. S. Ultrathin single-crystalline silver nanowire arrays formed in an ambient solution phase. *Science* **294,** 348–351 (2001).
19. Fujita, J., Ohnishi, Y., Ochiai, Y. & Matsui, S. Ultrahigh resolution of calixarene negative resist in electron beam lithography. *Appl. Phys. Lett.* **68,** 1297–1299 (1996).
20. Goldstein, D. J. Resolution in light microscopy studied by computer simulations. *J. Microsc.* **166,** 185–197 (1992).
21. Taflove, A. & Hagness, S. C. *Computational Electrodynamics: The Finite-difference Time-domain Method* (Artech House, 2000).
22. Simpson, G. J. Biological imaging: the diffraction barrier broken. *Nature* **440,** 879–880 (2006).
23. Lewis, A. *et al.* Near-field optics: from subwavelength illumination to nanometric shadowing. *Nature Biotechnol.* **21,** 1378–1386 (2003).
24. Smith, D. R., Pendry, J. B. & Wiltshire, M. C. K. Metamaterials and negative refractive index. *Science* **305,** 788–792 (2004).
25. Parimi, P. V., Lu, W. T., Vodo, P. & Sridhar, S. Photonic crystals: imaging by flat lens using negative refraction. *Nature* **426,** 404 (2003).
26. Chatterjee, R. *et al.* Achieving subdiffraction imaging through bound surface states in negative refraction photonic crystals in the near-infrared range. *Phys. Rev. Lett.* **100,** 187401 (2008).
27. Novoselov, K. S. *et al.* Electric field effect in atomically thin carbon films. *Science* **306,** 666–669 (2004).
28. Kim, K. S. *et al.* Large-scale pattern growth of graphene films for stretchable transparent electrodes. *Nature* **457,** 706–710 (2009).

Supplementary Information is linked to the online version of the paper at www.nature.com/nature.

Acknowledgements We thank T. F. Heinz, C. K. Hong, J. H. Lee and W. J. Kim for discussions, and K. Cho, J. T. Han, J. W. Lee and C. S. Lee for assisting in characterization. This work was supported by the Korea Foundation for International Cooperation of Science and Technology (Global Research Laboratory programme), Korea Science and Engineering Foundation grants funded by the Korea Government (World Class University, R32-2008-000-10180-0, R33-2008-000-10138-0; EPB Center, 2009-0063312; 2009-0062808; 2009-0060271), the Brain Korea 21 (Korea Research Foundation), the National Science Foundation (NSF: CHE-0641523; ECCS-0747787) and the New York State Office of Science (NYSTAR).

Author Contributions J.Y.L. and B.H.H. conducted experiments (synthesis, characterization, optical measurements). Y.K. assisted in synthesis. R.B., B.H.H. and C.W.W. conducted electromagnetic simulations, and W.Y.K., S.K.M. and M.V.J. analysed the simulation results. L.J.K. assisted in the high-resolution optical imaging analysis. I.-C.H. conducted lens transfer and lens array formation. Keun S. Kim and J.Y.L. obtained micro-Raman spectra. P.K. supervised optical measurements. Kwang S. Kim supervised the whole project.

Author Information Reprints and permissions information is available at www.nature.com/reprints. Correspondence and requests for materials should be addressed to Kwang S. Kim (kim@postech.ac.kr) or P.K. (pkim@phys.columbia.edu).